

High-gain optical parametric amplification with continuous-wave pump using domain-engineered thin film lithium niobate waveguide

Mengwen Chen¹, Chenyu Wang¹, Kunpeng Jia^{1,*}, Xiao-Hui Tian^{1,*}, Jie Tang², Chunxi Zhu¹, Xiaowen Gu², Zexing Zhao¹, Zikang Wang¹, Zhilin Ye^{1,3}, Ji Tang^{1,3}, Yong Zhang¹, Zhong Yan^{3,4}, Guang Qian², Biaobing Jin^{1,5}, Zhenlin Wang¹, Shi-Ning Zhu¹ and Zhenda Xie^{1,*}

¹ National Laboratory of Solid State Microstructures, School of Electronic Science and Engineering, College of Engineering and Applied Sciences, School of Physics, Research Institute of Superconductor Electronics (RISE) & Key Laboratory of Optoelectronic Devices and Systems with Extreme Performances of MOE, and Collaborative Innovation Center of Advanced Microstructures, Nanjing University, Nanjing 210093, China

² National Key Laboratory of Solid-State Microwave Devices and Circuits, Nanjing Electronic Devices Institute, Nanjing 210016, China

³ Nanzhi Institute of Advanced Optoelectronic Integration, Nanjing 211800, China

⁴ School of Integrated Circuits, Nanjing University of Information Science and Technology, Nanjing 210044, China

⁵ Purple Mountain Laboratories, Nanjing 211111, China.

* Correspondence: jiakunpeng@nju.edu.cn; tianxiaohui@nju.edu.cn; xiezhenda@nju.edu.cn

Abstract: While thin film lithium niobate (TFLN) is known for efficient signal generation, on-chip signal amplification remains challenging from fully integrated optical communication circuits. Here we demonstrate the first continuous-wave-pump optical parametric amplification (OPA) using an x-cut domain-engineered TFLN waveguide, with high gain over the telecom band up to 13.9 dB, and test it for high signal-to-noise ratio signal amplification using a commercial optical communication module pair. Fabricated in wafer scale using common process as devices including modulators, this OPA device marks an important step in TFLN photonic integration.

The recent development of information technology not only requires high-speed communication, but also calls for integrated optical communication devices, for applications including data center communication [1–3], satellite networks [4,5], integrated photonic processors [6,7], and optical integrated sensing and communication (O-ISAC) [8–10]. In recent years, thin film lithium niobate (TFLN) devices keep setting new records on the modulation speed and the low power consumption per bit [11–14], in a chip-scale footprint, which is beneficial for the further integration towards a compact optical communication device. Such integration not only relies on the linear optical devices, as demonstrated using TFLN before [15–19], but also relies on the on-chip optical signal amplification. Because this optical signal amplification is to fulfill the fundamental signal-to-noise ratio (SNR) requirement against optical losses [20,21], following the general Shannon-Hartley theorem. The most popular off-chip solution for optical signal amplification is the use of erbium-doped fiber amplifiers (EDFAs) [22,23], which inevitably increases the size of the system. The similar concept can be adapted to on-chip devices, by the laser-active doping in TFLN. However, these laser-active devices are fabricated from doped lithium niobate crystals before the smart cut process so far [24–29], and thus the whole TFLN chip has to be doped with the same ion density, which limits the performances of the non-laser-active devices including high-speed electro-optic modulators (EOMs).

On the other hand, optical parametric amplification (OPA) is an attractive alternate for the signal amplification [30,31], and known for its potential high gain and low noise for decades. Being a nonlinear optical process, a normal OPA requires high power to achieve high parametric gain, and thus most OPA experiments are pulse pumped [32,33], making them difficult to be used for effective communication signal amplification. The TFLN device confines light in small mode field size for much stronger nonlinearity compared to bulk material [34,35], and thus offers the new opportunity for the practical OPA of the communication signal, i.e., with continuous wave (CW) pump. However, fabricating an OPA device in TFLN that can achieve net parametric gain with a CW pump remains challenging.

Here we demonstrate the first high-gain OPA with CW pump on a TFLN chip. Cascaded second-harmonic generation (SHG) and OPA processes are used for an indirect-pump geometry, which greatly simplifies pumping condition and coupling design. High on-chip parametric gain has been measured with a broad 110 nm 10-dB bandwidth, covering both C and L bands at telecom wavelength, with gain up to 13.9

dB. Such OPA device has been tested for the optical communication signal amplification with commercial communication modules, at data rates from 200 to 1000 Mbps, with suppressed bit error rate (BER) below 10^{-2} . These results are achieved because of the high-quality fabrication of domain-engineered TFLN waveguides with both high nonlinearity and low optical loss simultaneously for the first time, using deep-ultraviolet (DUV) lithography method over an x-cut TFLN wafer. The ion-beam trimming technology is used for eliminating thickness variation influence in nonlinearity, and an etching-prior-poling process is used to reduce optical loss. This fabrication shares a common process as for the high-performance EOMs and other passive wafer-scale devices. Therefore, these results add the on-chip amplification capability of TFLN photonics and mark an important step towards fully integrated TFLN optical communication circuits.

We fabricate the OPA devices on an x-cut TFLN wafer, which is compatible with the fabrication of EOMs and other high-performance TFLN devices, as reported in many works before [14,36,37]. Instead of direct pumping, we use cascaded processes for the OPA demonstration, where the pump is indirectly generated on chip via an SHG process, so that only telecom-band fundamental wave (FW) input is necessary besides the signal light, as illustrated in Fig. 1(a). These two processes are designed to be phase-matched for the fundamental modes, i.e., TE_{00} in this case, in the waveguide, as shown in Eq. (1). Both the SHG and the OPA can be quasi-phase matched (QPM) using the same period Λ via domain engineering in a TFLN waveguide.

$$\begin{aligned} 2\omega_{FW, TE_{00}} &\rightarrow \omega_{p, TE_{00}} \text{ (SHG)}, \\ \omega_{p, TE_{00}} + \omega_{s, TE_{00}} &\rightarrow 2\omega_{s, TE_{00}} + \omega_{i, TE_{00}} \text{ (OPA)}, \end{aligned} \tag{1}$$

where $\omega_{j, TE_{00}}$ ($j = FW, p, s, i$) corresponds to the angular frequency for FW, pump, signal and idler light, respectively.

With this scheme, the input coupling only need to be optimized for the FW light at telecom wavelength. More importantly, such indirect pumping scheme enables deterministic excitation for the short-wavelength pump light in the fundamental mode as shown in Eq. (1). In a normal direct pumping scheme, however, it can be challenging for the coupling design to achieve high efficiency excitation of fundamental mode, considering the TFLN waveguide is multi-mode at short-wavelength pump.

It is also interesting to engineer a broad bandwidth of an OPA device, to fulfill the general requirement of the optical signal amplification. The bandwidth of OPA is

determined by the phase matching [38,39]. For an interaction length of l , the phase mismatch $\Delta\varphi$ related to the frequency detuning $\Delta\omega$ can be given by

$$\Delta\varphi = l(k_p - k_s - k_i - 2\pi/\Lambda) - l\beta_2(\Delta\omega)^2 - 2l \sum_{m=2}^{\infty} \frac{\beta_{2m}}{(2m)!} (\Delta\omega)^{2m}, \quad (2)$$

where k_j ($j = p, s, i$) is the wave vector for pump, signal and idler light, respectively. In the first order approximation, it is inversely proportional to the group velocity dispersion (GVD) β_2 . Thus, near-zero β_2 is designed for a large bandwidth of OPA.

With the sub-wavelength mode confinement in TFLN waveguide, the dispersion and QPM condition are sensitive to dimensions in cross-section. Specifically, the current TFLN wafers are normally fabricated with total thickness variation (TTV) on the order of tens-of-nanometers, and thus dramatically change the phase matching and reduce the parametric gain [40]. This is a crucial challenge to achieve high overall nonlinear efficiency from domain-engineered TFLN waveguides, even though high length-normalized nonlinear efficiency can be easily calculated using very short waveguides [41–44]. For individual device fabrication, adaptive poling can be an effective method for mapping thickness variation Δt along waveguide and patterning poling periods accordingly [45]. In this work to enable efficient wafer-scale fabrication, however, we have to push the Δt control over the TFLN wafer. We use the ion-beam trimming technique to actively trim the TFLN surface at nanometer level. As a result, the central area of the wafer can be trimmed within sub-10 nm Δt , while the Δt in the edges can be too large from a perfect trimming. Still, we can achieve about 2 nm root mean value (RMS) for Δt along waveguides with centimeter length in the central area.

Efficient OPA with CW pump also requires both high nonlinearity and low optical loss, simultaneously. Normally, domain engineering is achieved in a poling-prior-etching fabrication process. However, the selective etching can occur during the waveguide fabrication [46], forming steps on the waveguide surfaces following the domain walls, and inevitably increases the optical loss. We develop a different approach, etching-prior-poling process, to enable state-of-the-art wafer-scale fabrication of domain-engineered TFLN waveguides. The fabrication procedure is shown in Fig.1(b). The patterning of both waveguides and poling electrodes is achieved using DUV lithography in step-by-step process with high precision overlay alignment in-between, over an ion-trimmed, 4-inch, 600-nm-thick x-cut TFLN wafer.

The first step is for the waveguide fabrication, with an inverse-taper-type edge coupler on each end of the waveguide, to expand the sub-micron waveguide mode size for efficient coupling. The DUV exposure field size is $15 \times 16 \text{ mm}^2$ for one shot, which results in 21 chips from a single wafer. After the DUV patterning, the waveguide is fabricated using argon ions reactive ion etching. The second step is for the domain engineering over the existing waveguides. To achieve high-quality poling in this etching-prior-poling process, we optimize the poling electrodes design considering the waveguide cross-section profile. The electrodes are deposited with a 40-nm-thick Au layer stacked over a 30-nm-thick Cr layer, via electron-beam evaporation, and shaped in a lift-off process. A photograph of wafer after electrode fabrication is shown in Fig. 1(c). High-voltage poling [47] is then applied to waveguides for domain-engineering over the whole wafer. Domain-engineered waveguides with high-quality poling and smooth sidewalls over domains are achieved as shown in the left and right panels of Fig. 1(d). The duty cycle is near 50:50 for a small period of $4.17 \text{ }\mu\text{m}$. A 2- μm -thick SiO_2 cladding is then deposited via plasma-enhanced chemical vapor deposition, DUV patterned, and etched to form the inverse-taper-type edge coupler. The chips are finally separated by dicing, grinding, and polishing based on alignment marks. We measure the dimensions in the waveguide cross-section using SEM, for thickness t , top width w and slab thickness s of 594 nm, 1210 nm and 311 nm, respectively, and TE_{00} mode profiles are simulated using the measured dimensions, as shown in Fig. 1(e). The dispersion β_2 is then calculated to be $0.25 \text{ ps}^2/\text{m}$ around the signal wavelength, as shown in Fig. 1(f), which corresponds to a 110 nm 10-dB bandwidth of OPA.

We first measure the insertion losses of waveguides in a fiber-in and fiber-out setup, for ones with and without domain-engineering in comparison. Both types of waveguides show consistent insertion losses of $4.1 \pm 0.3 \text{ dB}$ in C-band, and such insertion losses stay relatively stable for different waveguide lengths from 2 mm to 12.3 mm. A low propagation loss on the order of 0.1 dB/cm can be derived, as expected by the use of etching-prior-poling process.

The 12.3-mm-long domain-engineered waveguides are designed for the OPA experiment. Using a low-power CW tunable laser (TSL-550, Santec) as the FW light, we measure their SHG performances in comparison from chip to chip. Fig. 2(a) shows the typical SHG measurement results from waveguides at different locations of the same wafer. In chips #6, #10, and #11 with low Δt from the central part, peak normalized efficiencies are measured from 1610 to 1790 $\%/\text{W}/\text{cm}^2$, with

corresponding peak overall efficiencies from 2440 to 2710 %/W. While in chips #1 and #3 with much higher Δt from the edge part, much lower efficiencies are measured at about 1600 %/W. We choose the waveguide from chip #10 for the OPA experiment.

Strong on-chip pump power is required for high-gain OPA. We use an EDFA to boost the power of FW light and measure its depletion at the output side, for the indirect measurement of on-chip pump power, which is free from the errors caused by the coupling effects. The strong near-infrared light can be observed using a camera while we increase the FW power, and Fig. 2(b) shows the picture of the chip with the shining waveguide. With the off-chip FW power set at 33.6 dBm, its depletion as a function of FW wavelength is shown in Fig. 2(c). A maximum depletion of about 90% can be measured at the phase matching wavelength of 1572 nm, indicating a maximum on-chip SHG efficiency of about 90%.

Then we are ready for the OPA experiment. The setup is schematically shown in Fig. 3(a). The OPA chip is placed on a temperature-controlled metal mount, with temperature stability of 2 mK. The FW light is from the amplified tunable laser as discussed above, and a pair of narrow bandpass filters (FBH1570-12, Thorlabs) are used to filter out the amplified spontaneous emission noise from the EDFA. The FW light is then combined with the signal light on a dichroic mirror, and coupled into the OPA chip with an aspherical lens. Two sets of $\lambda/2$ and $\lambda/4$ waveplates are used to independently adjust the polarization of FW and signal light, respectively. At the output side, we use a lensed fiber to collect the output of OPA chip. The lensed fiber is connected to a directional coupler (99:1), with its 1% output port to a silicon photodiode (S150C, 350 nm-1100 nm, Thorlabs) for monitoring the residual pump light, and 99% output port to an optical spectrum analyzer (OSA, AQ6374, YOKOGAWA) for spectral analysis. A spatial grating filter system, with an isolation of over 80 dB, is inserted before the OSA to prevent any residual high-power FW light from affecting the spectral detection.

The OPA performance is first tested with a CW signal input from a tunable laser (TSL-550, Santec). We initially turn off the FW light and couple only the signal light into the OPA chip. The output spectrum of OPA chip is recorded using OSA, as shown in Fig. 3(b) (solid brown curve). We then turn on the FW light with an off-chip power of 33.6 dBm. Obvious increase in signal power is observed in the spectrum, indicating the occurrence of amplification (Fig. 3(b)). By comparing the signal power with and

without the FW light, i. e., with and without OPA, the on-chip gain can be derived to be 13.9 dB, corresponding to a net gain of 9.9 dB considering the insertion loss of 4 dB. The generated conjugate idler light is also observed in the spectrum. The power level of the idler light is measured to be comparable to that of the signal light (< 0.2 dB), due to the intense OPA. We further test the SNR performance of the amplified signal light under different optical bandwidth settings, to simulate channels with different baud rates. Within the optical bandwidth ranging from 20 GHz to 200 GHz, the values of SNR consistently exceed 28 dB, peaking at 36 dB for the 20 GHz setting.

The OPA gain varies with the signal wavelength due to the change of the phase matching condition. We measure the on-chip gain at different signal wavelength in the range from 1520 nm to 1630 nm. The results are shown in the upper panel of Fig. 3(c), with the corresponding spectra shown below. The measured 10-dB bandwidth of OPA is over 100 nm, covering the whole telecom C and L bands, which is attributed to our dispersion engineering. It can also be seen that the FW light spectrum only occupies a small portion in the large bandwidth of OPA, forming a narrow rejection band. In this high-gain OPA process, vacuum quantum fluctuations are amplified to a macroscopic level through optical parametric generation (OPG). This results in a flat spectrum of OPG at the base of spectra in Figs. 3(b) and 3(c).

It is interesting to test the amplification of modulated signals for optical communication, using our OPA device. The modulated signals are from a pair of commercial optical communication modules. These signals are modulated in quadrature amplitude modulation (QAM) format. The experimental setup is illustrated in Fig. 4(a). The modulated signal light, from Alice (the transmitter), goes through our OPA device and single mode fiber (SMF) to Bob (the receiver). The presence or absence of OPA gain is controlled by the off-chip FW input. When the FW light is injected to the OPA chip, the modulated signal light can be amplified. We test the BER performances at data rates ranging from 200 Mbps to 1000 Mbps, with different input signal powers.

The BER test results, are illustrated in Fig. 4(b), for both the cases with and without OPA gain. The amplified signals with OPA gain consistently show several times lower BER results, than that of the cases without OPA gain. Notably, with OPA gain, signals as low as -44 dBm are successfully elevated to be above the detection threshold. A low BER result is still maintained to comply with communication standards. In contrast, without OPA gain, the sensitivity of optical modules restricts communication

capabilities for signals below -32 dBm. These results underscore the exceptional low-distortion amplification capabilities of our OPA device, attributed to its high gain. Such performance is essential for modern communication with high-capacity information demands, as it ensures the stability of high-speed data links. Note that the electro-optic modulation for encoding the data can be further realized by on-chip EOMs, and integrated with our OPA device towards fully integrated communication circuits.

In summary, we report the first high-gain OPA with CW pump using the TFLN waveguide. With up to 13.9 dB on-chip gain over a broad telecom band, high-fidelity signal amplification is performed, with the BER significantly below 10^{-2} for data rates ranging from 200 to 1000 Mbps. These results mark a cornerstone for fully integrated optical communication circuits. The OPA device is fabricated via our state-of-the-art wafer-scale fabrication of domain-engineered TFLN waveguides, which demonstrates a critical combination of high nonlinearity, low optical loss, broad bandwidth and high power handling capability, being ready for further integration with other TFLN devices, such like high-performance EOMs [36,37,48].

Currently, our OPA device requires watt-level off-chip FW power. The major limit on reducing power consumption is from the existing few nanometer-level TTV over the TFLN wafer, which prevents us from using longer waveguide for higher overall efficiency in this demonstration. However, this is not a fundamental limit because the better TTV can be expected by improving the smart-cut technology or further developing the higher-precision ion-beam trimming technique. In a 100-mm-long TFLN waveguide with Δt value of sub-1 nm, our simulation shows that power consumption below 100 mW is enough for even higher gain over 40 dB, which is within the power budget over single-mode semiconductor laser diode. A pump-integrated OPA device can thus be expected to utilize hybrid integration technology. For simplicity, we focus on the phase insensitive amplification (PIA) demonstration, by the combination of two identical waveguides, we can demonstrate phase sensitive amplification (PSA) [49,50] to fully reveal the high SNR advantage below the traditional quantum limit, which is not available using the normal amplifiers like EDFAs.

Such on-chip OPA device, either standing alone or integrated into optical communication circuits, paves the way for a wide range of applications in high-speed integrated optical communication [51,52], integrated photonic processors [53,54], photonic computing [55–58] and microwave photonics [59–61].

Acknowledgements

This work was supported by National Key R&D Program of China (2022YFA1205100, 2019YFA0705000, 2023YFB2805700), National Natural Science Foundation of China (62293523, 62293520, 12304421, 12341403), Leading-edge technology Program of Jiangsu Natural Science Foundation (BK20192001), Zhangjiang Laboratory (ZJSP21A001), Guangdong Major Project of Basic and Applied Basic Research (2020B0301030009), Program of Jiangsu Natural Science Foundation (BK20230770, BK20232033).

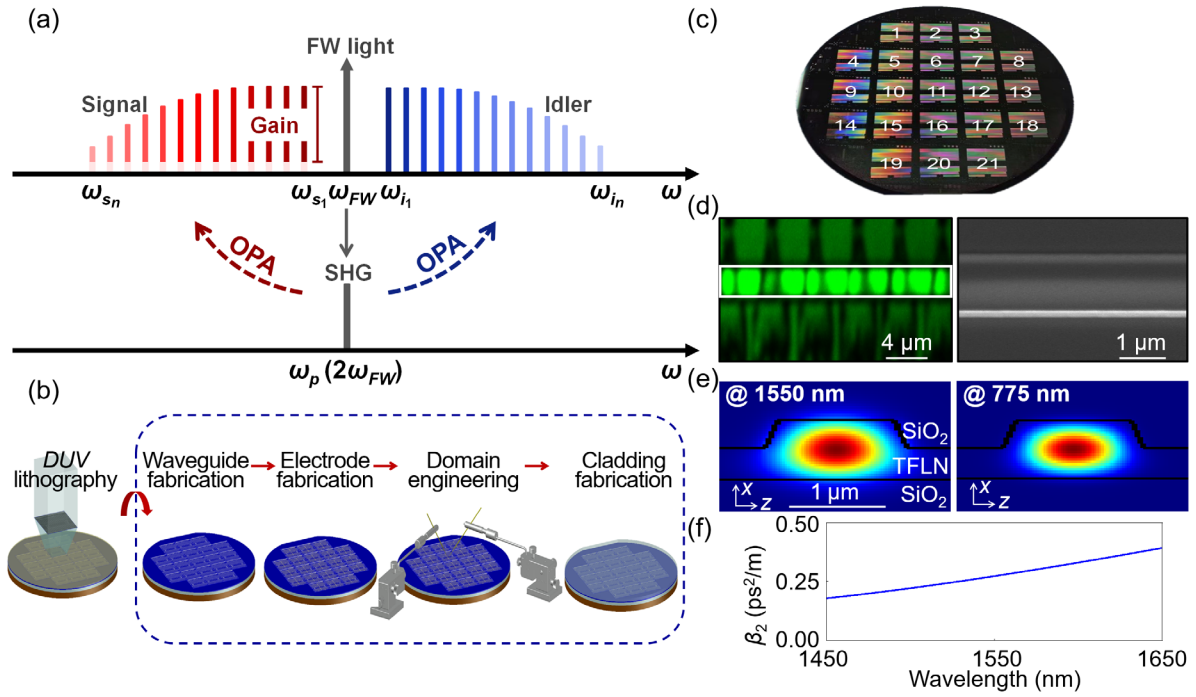


FIG. 1. (a) Diagrammatic depiction of the cascaded SHG and OPA processes. (b) Fabrication procedure of the OPA device. (c) Photograph of the wafer after electrode fabrication. (d) Left: confocal microscope image for domain-engineered waveguide. Right: SEM image of the waveguide from the top view. (e) Schematic of the waveguide cross section. (f) Calculated waveguide dispersion.

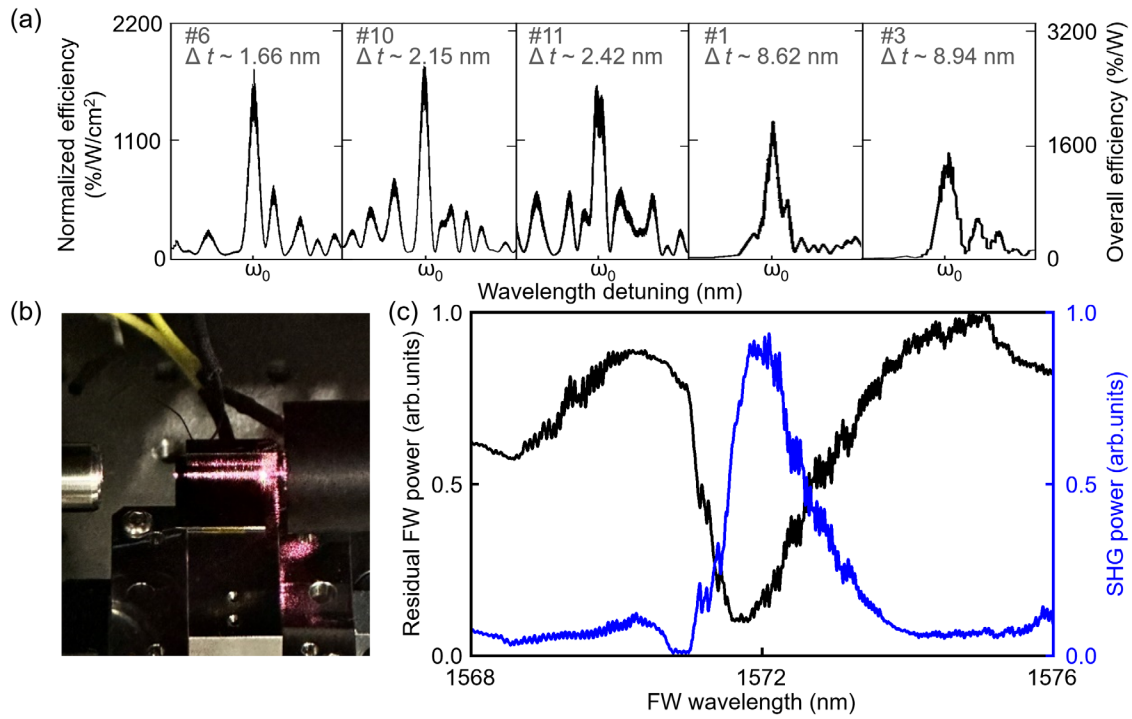


FIG. 2. (a) Typical SHG results of waveguides from different chips, with different Δt . (b) Picture of the OPA chip with the shining waveguide. (c) Residual FW power and generated SHG power as a function of FW wavelength.

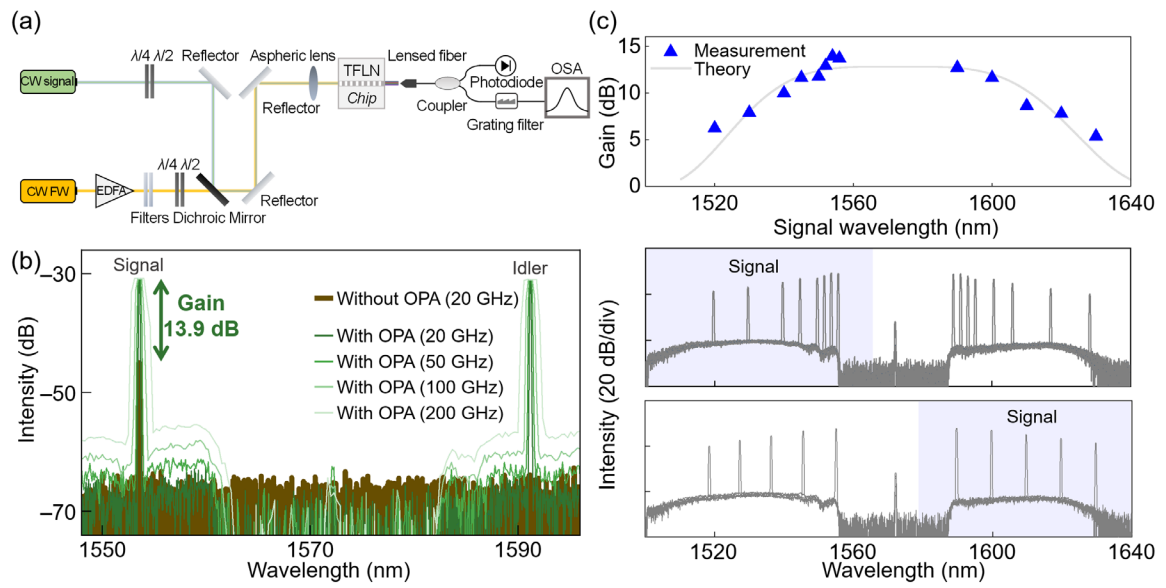


FIG. 3. (a) Experimental setup for CW-pumped OPA. (b) Output spectra of OPA chip. (c) On-chip gain as a function of signal wavelength. The corresponding spectra are shown below.

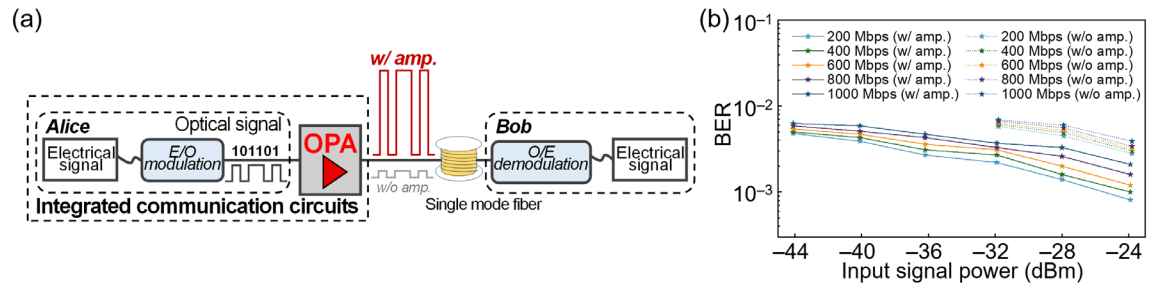


FIG. 4. (a) Experimental setup for modulated signal amplification. (b) BER as a function of input signal power.

- [1] Y. Hao et al., Recent progress of integrated circuits and optoelectronic chips, *Sci. China Inf. Sci.* **64**, 201401 (2021).
- [2] C. Lam, Hong Liu, B. Koley, Xiaoxue Zhao, V. Kamalov, and V. Gill, Fiber optic communication technologies: What's needed for datacenter network operations, *IEEE Commun. Mag.* **48**, 32 (2010).
- [3] Xiaoxue Zhao, V. Vusirikala, B. Koley, V. Kamalov, and T. Hofmeister, The prospect of inter-data-center optical networks, *IEEE Commun. Mag.* **51**, 32 (2013).
- [4] Y.-A. Chen et al., An integrated space-to-ground quantum communication network over 4,600 kilometres, *Nature* **589**, 214 (2021).
- [5] X. Zhu and C. Jiang, Integrated Satellite-Terrestrial Networks Toward 6G: Architectures, Applications, and Challenges, *IEEE Internet of Things Journal* **9**, 437 (2022).
- [6] P. I. Sund et al., High-speed thin-film lithium niobate quantum processor driven by a solid-state quantum emitter, *Sci. Adv.* **9**, eadg7268 (2023).
- [7] S. SeyedinNavadeh, M. Milanizadeh, F. Zanetto, G. Ferrari, M. Sampietro, M. Sorel, D. A. B. Miller, A. Melloni, and F. Morichetti, Determining the optimal communication channels of arbitrary optical systems using integrated photonic processors, *Nat. Photon.* **18**, 149 (2024).
- [8] H. He, L. Jiang, Y. Pan, A. Yi, X. Zou, W. Pan, A. E. Willner, X. Fan, Z. He, and L. Yan, Integrated sensing and communication in an optical fibre, *Light Sci Appl* **12**, 25 (2023).
- [9] F. Liu, Y. Cui, C. Masouros, J. Xu, T. X. Han, Y. C. Eldar, and S. Buzzi, Integrated Sensing and Communications: Toward Dual-Functional Wireless Networks for 6G and Beyond, *IEEE Journal on Selected Areas in Communications* **40**, 1728 (2022).
- [10] Z. Wei, H. Qu, Y. Wang, X. Yuan, H. Wu, Y. Du, K. Han, N. Zhang, and Z. Feng, Integrated Sensing and Communication Signals Toward 5G-A and 6G: A Survey, *IEEE Internet of Things Journal* **10**, 11068 (2023).
- [11] M. He et al., High-performance hybrid silicon and lithium niobate Mach–Zehnder modulators for 100 Gbit s⁻¹ and beyond, *Nat. Photonics* **13**, 359 (2019).
- [12] M. Xu et al., High-performance coherent optical modulators based on thin-film lithium niobate platform, *Nat Commun* **11**, 3911 (2020).
- [13] Hu Y. et al., Integrated electro-optics on thin-film lithium niobate, <https://arxiv.org/abs/2404.06398v2>.
- [14] N. Chen, K. Lou, Y. Yu, X. He, and T. Chu, High-Efficiency Electro-Optic Modulator on Thin-Film Lithium Niobate with High-Permittivity Cladding, *Laser & Photonics Reviews* **17**, 2200927 (2023).
- [15] J. Lin, F. Bo, Y. Cheng, and J. Xu, Advances in on-chip photonic devices based on lithium niobate on insulator, *Photon. Res.* **8**, 1910 (2020).
- [16] Y. Qi and Y. Li, Integrated lithium niobate photonics, *Nanophotonics* **9**, 1287 (2020).
- [17] Y. Jia, L. Wang, and F. Chen, Ion-cut lithium niobate on insulator technology: Recent advances and perspectives, *Applied Physics Reviews* **8**, 011307 (2021).
- [18] A. Boes, L. Chang, C. Langrock, M. Yu, M. Zhang, Q. Lin, M. Lončar, M. Fejer, J. Bowers, and A. Mitchell, Lithium niobate photonics: Unlocking the electromagnetic spectrum, *Science* **379**, eabj4396 (2023).
- [19] A. Boes, B. Corcoran, L. Chang, J. Bowers, and A. Mitchell, Status and Potential of Lithium Niobate on Insulator (LNOI) for Photonic Integrated Circuits, *Laser & Photonics Reviews* **12**, 1700256 (2018).

- [20] R.-J. Essiambre, G. Kramer, P. J. Winzer, G. J. Foschini, and B. Goebel, Capacity Limits of Optical Fiber Networks, *J. Lightwave Technol.* **28**, 662 (2010).
- [21] R. I. Killey and C. Behrens, Shannon's theory in nonlinear systems, *Journal of Modern Optics* **58**, 1 (2011).
- [22] D. R. Zimmerman and L. H. Spiekman, Amplifiers for the Masses: EDFA, EDWA, and SOA Amplets for Metro and Access Applications, *J. Lightwave Technol.* **22**, 63 (2004).
- [23] H. Masuda and S. Kawai, Wide-band and gain-flattened hybrid fiber amplifier consisting of an EDFA and a multiwavelength pumped Raman amplifier, *IEEE Photon. Technol. Lett.* **11**, 647 (1999).
- [24] Y. Zhang, Q. Luo, D. Zheng, S. Wang, S. Liu, H. Liu, F. Bo, Y. Kong, and J. Xu, Highly efficient on-chip erbium–ytterbium co-doped lithium niobate waveguide amplifiers, *Photon. Res.* **11**, 1733 (2023).
- [25] Z. Zhang et al., Erbium-ytterbium codoped thin-film lithium niobate integrated waveguide amplifier with a 27 dB internal net gain, *Opt. Lett.* **48**, 4344 (2023).
- [26] M. Cai, K. Wu, J. Xiang, Z. Xiao, T. Li, C. Li, and J. Chen, Erbium-Doped Lithium Niobate Thin Film Waveguide Amplifier With 16 dB Internal Net Gain, *IEEE J. Select. Topics Quantum Electron.* **28**, 1 (2022).
- [27] J. Wu, X. Yan, X. Wang, T. Yuan, C. Chen, H. Li, Y. Chen, and X. Chen, Efficient Integrated Amplifier-Assisted Laser on Erbium-Doped Lithium Niobate, *ACS Photonics* **11**, 2114 (2024).
- [28] Z. Chen, Q. Xu, K. Zhang, W.-H. Wong, D.-L. Zhang, E. Y.-B. Pun, and C. Wang, Efficient erbium-doped thin-film lithium niobate waveguide amplifiers, *Opt. Lett.* **46**, 1161 (2021).
- [29] Y. Jia, J. Wu, X. Sun, X. Yan, R. Xie, L. Wang, Y. Chen, and F. Chen, Integrated Photonics Based on Rare-Earth Ion-Doped Thin-Film Lithium Niobate, *Laser & Photonics Reviews* **16**, 2200059 (2022).
- [30] D. Sun, Y. Zhang, D. Wang, W. Song, X. Liu, J. Pang, D. Geng, Y. Sang, and H. Liu, Microstructure and domain engineering of lithium niobate crystal films for integrated photonic applications, *Light Sci Appl* **9**, 197 (2020).
- [31] M. G. Vazimali and S. Fathpour, Applications of thin-film lithium niobate in nonlinear integrated photonics, *AP* **4**, 034001 (2022).
- [32] M. Jankowski, N. Jornod, C. Langrock, B. Desiatov, A. Marandi, M. Lončar, and M. M. Fejer, Quasi-static optical parametric amplification, *Optica* **9**, 273 (2022).
- [33] L. Ledezma, R. Sekine, Q. Guo, R. Nehra, S. Jahani, and A. Marandi, Intense optical parametric amplification in dispersion-engineered nanophotonic lithium niobate waveguides, *Optica* **9**, 303 (2022).
- [34] A. Honardoost, K. Abdelsalam, and S. Fathpour, Rejuvenating a Versatile Photonic Material: Thin-Film Lithium Niobate, *Laser & Photonics Reviews* **14**, 2000088 (2020).
- [35] G. Chen, N. Li, J. D. Ng, H.-L. Lin, Y. Zhou, Y. H. Fu, L. Y. T. Lee, Y. Yu, A.-Q. Liu, and A. J. Danner, Advances in lithium niobate photonics: development status and perspectives, *AP* **4**, 034003 (2022).
- [36] Y. Zheng et al., Electro-optically programmable photonic circuits enabled by wafer-scale integration on thin-film lithium niobate, *Phys. Rev. Research* **5**, 033206 (2023).
- [37] Z. Li et al., High density lithium niobate photonic integrated circuits, *Nat Commun* **14**, 4856 (2023).
- [38] M. Jankowski, C. Langrock, B. Desiatov, A. Marandi, C. Wang, M. Zhang, C. R. Phillips, M.

- Lončar, and M. M. Fejer, Ultrabroadband nonlinear optics in nanophotonic periodically poled lithium niobate waveguides, *Optica* **7**, 40 (2020).
- [39] U. A. Javid, J. Ling, J. Staffa, M. Li, Y. He, and Q. Lin, Ultrabroadband Entangled Photons on a Nanophotonic Chip, *Phys. Rev. Lett.* **127**, 183601 (2021).
- [40] X.-H. Tian et al., Effect of dimension variation for second-harmonic generation in lithium niobate on insulator waveguide [Invited], *Chin. Opt. Lett.* **19**, 060015 (2021).
- [41] L. Chang, Y. Li, N. Volet, L. Wang, J. Peters, and J. E. Bowers, Thin film wavelength converters for photonic integrated circuits, *Optica* **3**, 531 (2016).
- [42] Y. Niu, C. Lin, X. Liu, Y. Chen, X. Hu, Y. Zhang, X. Cai, Y.-X. Gong, Z. Xie, and S. Zhu, Optimizing the efficiency of a periodically poled LNOI waveguide using *in situ* monitoring of the ferroelectric domains, *Appl. Phys. Lett.* **116**, 101104 (2020).
- [43] C. Wang, C. Langrock, A. Marandi, M. Jankowski, M. Zhang, B. Desiatov, M. M. Fejer, and M. Lončar, Ultrahigh-efficiency wavelength conversion in nanophotonic periodically poled lithium niobate waveguides, *Optica* **5**, 1438 (2018).
- [44] R. Luo, Y. He, H. Liang, M. Li, and Q. Lin, Highly tunable efficient second-harmonic generation in a lithium niobate nanophotonic waveguide, *Optica* **5**, 1006 (2018).
- [45] P.-K. Chen, I. Briggs, C. Cui, L. Zhang, M. Shah, and L. Fan, Adapted poling to break the nonlinear efficiency limit in nanophotonic lithium niobate waveguides, *Nat. Nanotechnol.* **19**, 44 (2024).
- [46] I. E. Barry, G. W. Ross, P. G. R. Smith, R. W. Eason, and G. Cook, Microstructuring of lithium niobate using differential etch-rate between inverted and non-inverted ferroelectric domains, *Materials Letters* **37**, 246 (1998).
- [47] M. Chen et al., Wafer-Scale Periodic Poling of Thin-Film Lithium Niobate, *Materials* **17**, 1720 (2024).
- [48] V. Snigirev et al., Ultrafast tunable lasers using lithium niobate integrated photonics, *Nature* **615**, 411 (2023).
- [49] S. L. I. Olsson, H. Eliasson, E. Astra, M. Karlsson, and P. A. Andrekson, Long-haul optical transmission link using low-noise phase-sensitive amplifiers, *Nat Commun* **9**, 2513 (2018).
- [50] Z. Tong, C. Lundström, P. A. Andrekson, C. J. McKinstrie, M. Karlsson, D. J. Blessing, E. Tipsuwannakul, B. J. Puttnam, H. Toda, and L. Grüner-Nielsen, Towards ultrasensitive optical links enabled by low-noise phase-sensitive amplifiers, *Nature Photon* **5**, 430 (2011).
- [51] C. Wang, M. Zhang, X. Chen, M. Bertrand, A. Shams-Ansari, S. Chandrasekhar, P. Winzer, and M. Lončar, Integrated lithium niobate electro-optic modulators operating at CMOS-compatible voltages, *Nature* **562**, 101 (2018).
- [52] E. Agrell et al., Roadmap on optical communications, *J. Opt.* **26**, 093001 (2024).
- [53] D. Zhu et al., Integrated photonics on thin-film lithium niobate, *Adv. Opt. Photon.* **13**, 242 (2021).
- [54] L. S. Madsen et al., Quantum computational advantage with a programmable photonic processor, *Nature* **606**, 75 (2022).
- [55] B. J. Shastri, A. N. Tait, T. Ferreira De Lima, W. H. P. Pernice, H. Bhaskaran, C. D. Wright, and P. R. Prucnal, Photonics for artificial intelligence and neuromorphic computing, *Nat. Photonics* **15**, 102 (2021).
- [56] Z. Ma, J.-Y. Chen, Z. Li, C. Tang, Y. M. Sua, H. Fan, and Y.-P. Huang, Ultrabright Quantum Photon Sources on Chip, *Phys. Rev. Lett.* **125**, 263602 (2020).

- [57] H. Jin, F. M. Liu, P. Xu, J. L. Xia, M. L. Zhong, Y. Yuan, J. W. Zhou, Y. X. Gong, W. Wang, and S. N. Zhu, On-Chip Generation and Manipulation of Entangled Photons Based on Reconfigurable Lithium-Niobate Waveguide Circuits, *Phys. Rev. Lett.* **113**, 103601 (2014).
- [58] P. Fisher, R. Cernansky, B. Haylock, and M. Lobino, Single Photon Frequency Conversion for Frequency Multiplexed Quantum Networks in the Telecom Band, *Phys. Rev. Lett.* **127**, 023602 (2021).
- [59] D. Marpaung, J. Yao, and J. Capmany, Integrated microwave photonics, *Nature Photon* **13**, 80 (2019).
- [60] X. Zou, B. Lu, W. Pan, L. Yan, A. Stöhr, and J. Yao, Photonics for microwave measurements, *Laser & Photonics Reviews* **10**, 711 (2016).
- [61] H. Feng et al., Integrated lithium niobate microwave photonic processing engine, *Nature* **627**, 80 (2024).